Acta Metallurgica Sinica (English Letters) (2024) 37:1657–1666
https://doi.org/10.1007/s40195-024-01738-5

Atomistic Insights into the Irradiation Resistance of Co-Free High Entropy Alloy FeMnNiCr

Chunhui Wang[1] · Lei Guo[1] · Rui Li[1] · Qing Peng[2,3,4]

Received: 7 March 2024 / Revised: 8 April 2024 / Accepted: 17 April 2024 / Published online: 28 June 2024

Abstract
We have investigated the displacement cascade irradiation resistance behavior of a cobalt-free high entropy alloy FeMnNiCr using molecular dynamics simulations. The results show that defects in FeMnNiCr form in small clusters, and their migration is significantly inhibited, leading to a higher defect recombination rate and a lower number of residual defects compared to Ni. Additionally, FeMnNiCr exhibits a longer thermal peak life and lower thermal conductivity compared to Ni, providing a longer time for defect migration and combining. The migration of defect clusters in FeMnNiCr displays three-dimensional properties, attributed to its high chemical disorder. After prolonged irradiation, defects in FeMnNiCr stabilize as small clusters, whereas point defects in Ni tend to form large defect clusters and evolve into dislocations. Considering the feature of absence of the element cobalt, our results imply that FeMnNiCr has great potential in application in nuclear energies.

Keywords High entropy alloys · Displacement cascade · Irradiation defects · Molecular dynamics

1 Introduction

Nuclear energy, recognized as an efficient and clean energy source, is increasingly significant in the energy sector. Following nuclear energy technology advances, the prolonged exposure to high temperature and irradiation in nuclear reactors inevitably results in irradiation-induced damage to structural materials, characterized by elemental segregation, swelling, and hardening [1–3]. Consequently, this damage leads to a deterioration of the macroscopic mechanical properties [4–6]. The evolving demands for structural material performance [7], are such that the current zirconium alloys and austenitic stainless steels, despite their widespread application, are increasingly unable to meet these stringent criteria [8].

In recent years, high-entropy alloys (HEAs) [9, 10] consisting of four or more metal elements in equimolar or nearly equimolar ratios have received a lot of attention due to their excellent structural stability [11–15] and mechanical properties [16, 17], and are considered promising materials for next-generation reactor structure materials [18, 19]. High-entropy alloys have shown to exhibit superior performance compared to conventional alloys under irradiation. For example, Lu et al. [20] indicated that NiCoFeCrMn reduced pore size upon irradiation compared to Ni and NiCo. Yang et al. [21] applied helium ion irradiation on Ni, 304SS, and CrMnFeCoNi at 450 °C, revealing that CrMnFeCoNi had the best structural stability and helium resistance properties. Kumar et al. [22] compared the structure of FeNiMnCr with that of austenitic stainless steels FeNiCr and FeMnCr under Ni ion irradiation. The results showed that FeNiMnCr exhibited enhanced phase stability at temperature exceeding 400 °C, with a notable reduction in elemental segregation at grain boundaries.

Available online at http://link.springer.com/journal/40195.

✉ Rui Li
lirui@ustb.edu.cn

✉ Qing Peng
pengqing@imech.ac.cn

[1] School of Mechanical Engineering, University of Science and Technology Beijing, Beijing 100083, China

[2] State Key Laboratory of Nonlinear Mechanics, Institute of Mechanics, Chinese Academy of Sciences, Beijing 100190, China

[3] Center of Materials Science and Optoelectronics Engineering, University of Chinese Academy of Sciences, Beijing 100049, China

[4] Guangdong Aerospace Research Academy, Guangzhou 511458, China

Despite the experimental studies on the remarkable irradiation resistance of high-entropy alloys, the underlying mechanisms remain incompletely elucidated. The displacement cascade process of irradiation damage is extremely fast, in order of nanoseconds (10^{-9} s), and the evolution of defects and dislocations generated during the cascade is a phenomenon at atomic level. The atomic level defect evolution mechanism is challenging to elucidate solely through experimental approaches. It is also worth noting that numerous studies on other high-entropy alloys, such as NiCoFeCrMn [23–25], NiCoFeCrCu [26–28], NiCoCrFe [29–31], have also showed their superior irradiation resistance properties. However, the elements of the studied high-entropy alloys contain cobalt, an element with a high thermal neutron absorption cross-section. The long decay time associated with neutron activation [32] necessitates enhanced radiation shielding for post-irradiation treatment, potentially increasing the risk of radiation exposure during nuclear power plant maintenance [5, 22, 33]. Consequently, the elemental composition of high-entropy alloys should be optimized to ensure their stability and safety when they are employed as nuclear structure materials.

Research into the generation, progression, and mitigation of defects during the initial phases of irradiation cascades is deemed a valuable approach for elucidating the mechanisms underpinning material irradiation resistance [34]. Molecular dynamics (MD) simulations facilitate the atomic-scale modeling of the irradiation process, offering a robust platform for elucidating the microstructural mechanisms that confer irradiation resistance to high-entropy alloys [23, 35, 36]. Given that FeMnNiCr does not contain cobalt, it is possibly an ideal candidate for high-entropy alloys in nuclear structural applications. Recent studies on FeMnNiCr [5, 22, 32, 33, 37, 38] have been conducted, yet the literature is sparse regarding the microscopic mechanisms of its anti-irradiation properties, necessitating further investigation.

This study presents a series of displacement cascade simulations of FeMnNiCr with equal atomic ratios via molecular dynamics simulations, within a high-temperature irradiation environment at 600 K. The mechanisms governing defect generation and evolution during the cascade process of FeMnNiCr are examined and compared with those of Ni. The findings elucidate the factors contributing to the high irradiation tolerance of FeMnNiCr, thereby establishing a theoretical foundation for its potential use in nuclear reactor structure materials.

2 Methodology

2.1 Model Setup of the Cascade

In this study, molecular dynamics simulations of displacement cascades are performed using large-scale atomic/molecular massively parallel simulator (LAMMPS) software [39]. The modified embedded atom method (MEAM) potential function developed by Choi et al. [40] is selected for the FeMnNiCr model, which has been widely proved to be effective in describing the irradiation damage properties of high-entropy alloys [41], and in order to accurately simulate the cascade collisions of energetic ions, the Ziegler–Biersack–Littmark (ZBL) potential function [42] is to describe the atomic short-range forces during collisions and used in conjunction with the aforementioned potential function. The Ni model also employs the MEAM potential function to facilitate a comparison with the irradiation resistance of FeMnNiCr.

As shown in Fig. 1, FeMnNiCr and Ni models of size 80 $a_0 \times 80\ a_0 \times 80\ a_0$ are constructed, each containing 2048000 atoms. a_0 represents the lattice constant, which is taken to be 3.52 Å for the Ni, close to the experimental value [43]. The average lattice constant of the FeMnNiCr model, calculated

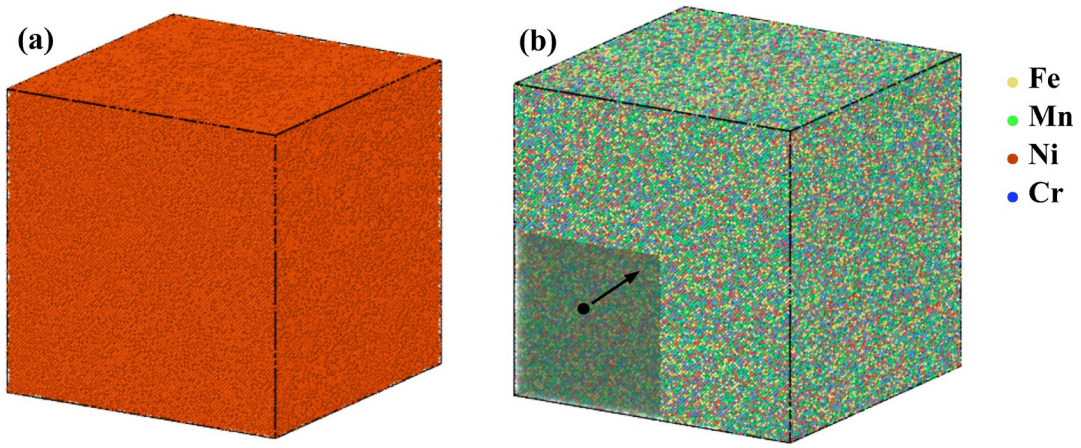

Fig. 1 Two displacement cascade models **a** Ni, **b** FeMnNiCr. The yellow, green, red, and blue balls represent Fe, Mn, Ni, and Cr, respectively

via energy minimization, is determined to be 3.552 Å. The FeMnNiCr model with a random distribution of equiatomic ratios is constructed based on the Ni model, which is formed according to the random replacement of Ni atoms for Fe, Mn, and Cr atoms.

Periodic boundary conditions are applied along three dimensions for both models to simulate the behavior of infinite large crystals. Before conducting the cascade, the system energy is optimized to a steady state using a conjugate gradient algorithm, followed by atomic relaxation at 600 K under isothermal-isobaric ensemble (NPT) ensemble for 15 picoseconds to achieve equilibrium.

The cascade process is conducted under canonical ensemble (NVT) ensemble, with temperature regulation facilitated by the Berendsen thermostat, employing an outermost layer 10 Å in thickness at 600 K to dissipate excess heat generated during the cascade. Furthermore, to limit the maximum atomic displacement during the cascade, an adaptive time-step algorithm is employed to guarantee that displacements in each time increment do not surpass 0.02 Å. The cascade is conducted by randomly selecting an atom as the primary knock-on atom (PKA), imparting it with an energy of 30 keV to obtain the initial velocity, and to avoid channeling, we choose the high-index direction [44] as the incidence direction of the PKA. The cascade process lasts 90 ps for the FeMnNiCr model, while for the Ni model, the duration of the cascade simulation is set to 60 ps due to its faster recovery to the equilibrium state. Meanwhile, considering the randomness of the PKA location and the disordered nature of the high-entropy alloy structure, we perform a total of 10 displacement cascade simulations for the two models to analyze the formation, migration, and combination process of the defects.

Moreover, we also simulate the accumulation of defects under long-term irradiation by introducing Frenkel pairs (FPs) at a concentration of 1% in a stochastic manner. The simulation process is as follows: initially, systems with preset defects are allowed to evolve naturally to the equilibrium. Subsequently, a PKA is randomly selected within the system, and a displacement cascade simulation is initiated to analyze the defect evolution.

2.2 Defect Analysis

The open source visualization software OVITO [45] is applied to analyze the generation, evolution, and distribution of defects during the cascade process. The interstitial atoms and vacancy defects generated during the cascade process are identified using Wigner–Seitz method [46]. The defects are categorized into clusters of different sizes according to the given truncation radius by Cluster analysis. Clusters containing 1–2 defects are defined as small clusters, those with 3–10 defects as medium clusters, and those with more than 10 defects as large clusters. Dislocation analysis (DXA) [47] is used to identify the dislocations generated during the displacement cascade.

2.3 Thermal Conductivity

The thermal conductivities of FeMnNiCr and Ni are calculated by the non-equilibrium molecular dynamics method (NEMD) [48]. A model with dimensions of 300 a_0×4 a_0×4 a_0 is constructed with a temperature gradient for a continuous simulation of 100 ps in order to simulate the heat transfer process. Subsequently, the thermal conductivities of two materials at a temperature of 600 K are calculated according to Eq. (1).

$$\kappa = \frac{-J}{A \times \nabla T}. \tag{1}$$

where J denotes the heat flow density. A is the cross-sectional area for heat transfer; and ∇T is the temperature gradient during heat transfer.

2.4 Migration Properties of Defect Clusters

Within a simulation cell of dimensions 20 a_0×20 a_0×20 a_0, an interstitial cluster composed of 9 atoms is modeled. Given the compositional complexity and inherent disorder in FeMnNiCr, the migration barrier is high, which hinders the mobility of defect clusters at equivalent temperatures. Consequently, we adjusted the simulation temperatures to 800 K for Ni and 1200 K for FeMnNiCr to observe the migration behavior of interstitial clusters in both materials.

3 Results and Discussion

3.1 Defect Generation and Cascade Evolution

Figure 2 illustrates the evolution of Frenkel Pairs formation in FeMnNiCr and Ni alloys during displacement cascades initiated by PKA with an initial energy of 30 keV. The FPs formation process in both alloys can be broadly categorized into three distinct stages: the initial rapid growth stage, where PKA transfer energy through collisions, inducing sub-cascades and a rapid rise in the number of FPs to a peak; the subsequent stage is the defect recombination stage, wherein numerous interstitial atoms interact with vacancy defects, leading to a gradual reduction in the number of FPs until a quasi-steady state is achieved; the final stage marks the onset of long-term diffusion, during which the number of FPs maintains a dynamic equilibrium. However, the evolution of defects in this phase is challenging to discern due to the constrained observation timeframe.

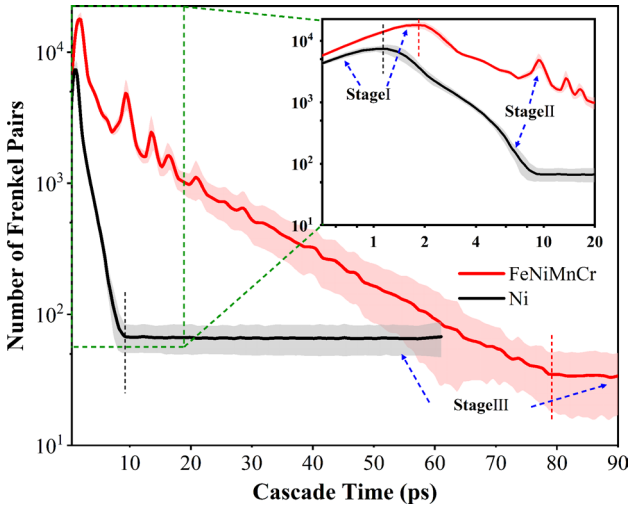

Fig. 2 Evolution of the number of FPs with respect to time during cascade displacement process for two materials, FeNiMnCr (red line) and Ni (black line), where the PKA energy is $E_{PKA}=30$ keV. The inset is the zoom-in of the plot within 20 ps. The Stage I and Stage II are marked

During the rapid growth stage, FeMnNiCr exhibits a delayed peak in FPs formation compared to Ni, yet surpasses Ni in terms of the number of FPs. As the system transits to the defect recombination phase, the number of FPs in Ni decreases swiftly, approaching equilibrium, whereas FeMnNiCr displays secondary peaks, a phenomenon observed by previous research [41, 49]. These secondary peaks occur due to shock waves reentering the MD cell through periodic boundaries, which only has slight influence on the cascade dynamics.

In order to describe the degree of defect recombination at the end of the cascade for the two materials, the defect recombination rate η is used to evaluate the defect recombination effect at the end of the cascade, with the following equation:

$$\eta = \frac{\mathrm{FPs}_{\mathrm{peak}} - \mathrm{FPs}_{\mathrm{stable}}}{\mathrm{FPs}_{\mathrm{peak}}}. \quad (2)$$

where $\mathrm{FPs}_{\mathrm{peak}}$ is the number of FPs at peak during the cascade process and $\mathrm{FPs}_{\mathrm{stable}}$ denotes the number of residual FPs in material at equilibrium. Table 1 shows the time and number of FPs reaching the peak and equilibrium states during the displacement cascade process of FeMnNiCr and Ni. The defect recombination rate of the two materials is calculated according to Eq. (2). The results show that the number of FPs at peak in FeMnNiCr is twice greater than that in Ni. Similarly, the similar composed high-entropy alloys also produced more defects than Ni during rapid growth stage, such as CoCrFeNiMn [41] and CoCrFeNi [29], which may be attributed to the lower atomic displacement energy of the high-entropy alloys. However, the evolution time of the cascade in FeMnNiCr during the defect recombination stage is significantly longer than that in Ni, and the number of residual FPs at equilibrium is less than that in Ni. FeMnNiCr exhibits a higher recombination rate, which leads to the better irradiation resistance properties of FeMnNiCr than Ni.

Table 1 Time, number of FPs, and defect recombination rate when reaching the cascade spike and steady state

Sample	Time to peak (ps)	Number of FPs at peak	Time to steady (ps)	Number of surviving FPs	Defect recombination rate
FeMnNiCr	1.77	17,970	79.12	34	99.81%
Ni	1.03	7347	10.34	67	99.08%

3.2 Defect Distribution and Dynamic Evolution

Figure 3 shows the spatial distribution of defects in FeMnNiCr (panels a-b) and Ni (panels c-d) at the thermal peak and the end of the cascade. In panels a and c, it is evident that defects in FeMnNiCr at the thermal peak are predominantly clustered, whereas in Ni, a notable migration of defects is observed. This disparity is accentuated at the end of cascade, as illustrated in panels b and d, with residual defects in FeMnNiCr remaining relatively concentrated. Kumar et al. [22] observed the limited increase of dislocation loop in FeNiMnCr under ion irradiation by experiments, which is consistent with our results. However, residual defects in Ni exhibit a more dispersed pattern, which mitigates the likelihood of interstitial atoms encountering and recombining with vacancies, leading to larger residual defects.

The size and number distribution of defect clusters in FeMnNiCr and Ni at the end of cascade is shown in Fig. 4. The majority of interstitial atoms in FeMnNiCr are in small clusters, typically comprising 1–2 atoms, with the aggregation into larger clusters being markedly suppressed. In contrast, in Ni, the small interstitial clusters exceed that in FeMnNiCr, and there is a greater propensity for interstitial atoms to evolve into stable, larger clusters. The fraction of larger interstitial clusters in FeMnNiCr is less than in Ni, with the largest clusters in FeMnNiCr being approximately one-third the size of those in Ni. This observation is corroborated by recent research conducted by Lu et al. and Lin et al. Lu et al. [20, 50] reported that experimentally irradiated Ni had larger interstitial clusters than HEA. Lin et al. [29] demonstrated that the size of interstitial clusters in Ni kept increasing, but those in HEA remained diminutive with the increase of irradiation dose through MD simulations. Collectively, both experimental and simulation findings reveal that the interstitial clusters in Ni under higher

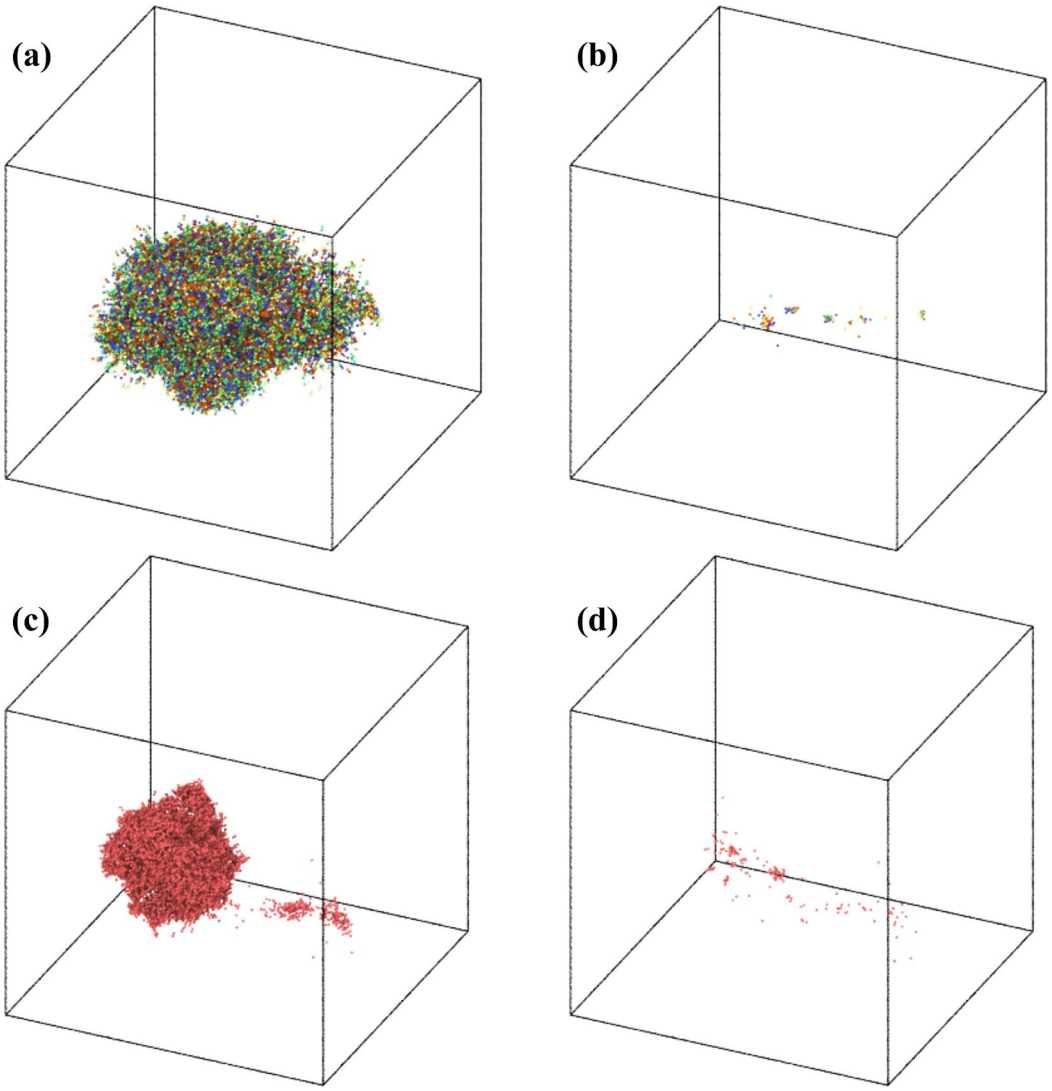

Fig. 3 Spatial distribution of defects at the thermal peak for **a** FeMnNiCr and **c** Ni, compared to that at the end of the cascade for **b** FeMnNiCr and **d** Ni

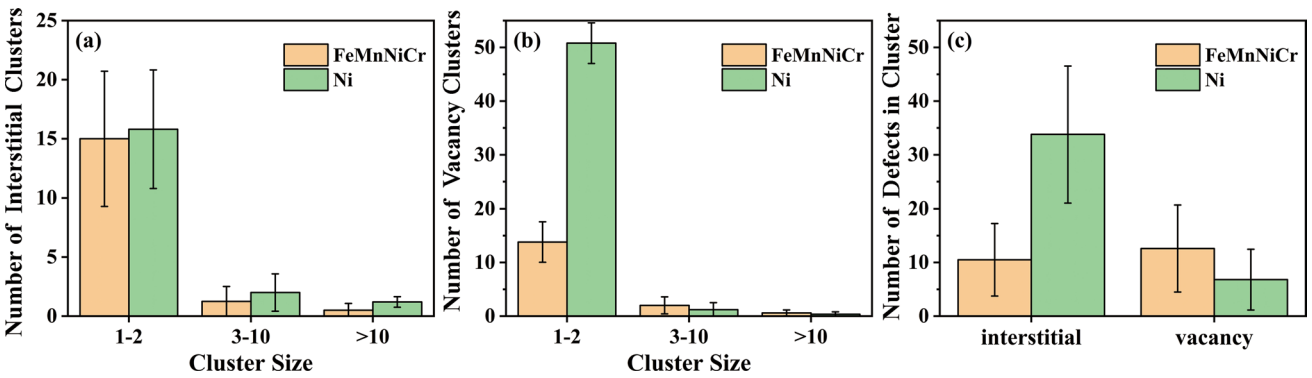

Fig. 4 Size distribution of defect clusters in FeMnNiCr (yellow) and Ni (green) at the end of cascade: **a** interstitial clusters, **b** vacancy clusters, **c** the largest defect clusters

irradiation conditions are considerably larger than those in HEA, aligning with the outcomes of this study.

Figure 4b indicates that, while the number of residual vacancy defects in FeMnNiCr is lower than in Ni, there exists a notable disparity in the size distribution of vacancy clusters between the two materials. It is evident that the vacancy defects in Ni predominantly form 1–2 atom clusters, which are significantly more numerous than those in FeMnNiCr. Conversely, the vacancy defects in FeMnNiCr are more prone to aggregating during the displacement cascades, leading to the emergence of medium to large-sized vacancy clusters, a pattern that aligns with experimental observations [51]. Nonetheless, the size of the largest vacancy clusters formed in both FeMnNiCr and Ni is generally modest, implying that the propensity for large vacancy cluster formation within the crystal lattices is mitigated.

3.3 Potential Energy and Temperature

To investigate the kinetic behavior of defects in FeMnNiCr during irradiation, we assess the potential energy of from the beginning to equilibrium of the cascade. As depicted in Fig. 5(a), at the beginning of the cascade, the PKA atom collides with other atoms, resulting in the potential energy of system rapidly climbing to the peak. Subsequently, the potential energy declines gradually, eventually reaching equilibrium after an extended period. Despite the identical initial kinetic energies of PKA atoms in both FeMnNiCr and Ni, the potential energy in Ni dissipates more rapidly, achieving equilibrium within 60 picoseconds. Nonetheless, the potential energy of FeMnNiCr remains unbalanced even after 90 picoseconds, even though the number of defects has reached a dynamic equilibrium. This suggests that the rate of energy dissipation in FeMnNiCr is markedly slower compared to Ni. Consequently, this extended time frame allows for additional defect evolution and promotes the encounter and recombination of interstitial atoms with vacancies.

Temperature is a critical determinant of the rate of energy dissipation and the migratory dynamics of defects. We have conducted a subsequent analysis of the system temperature throughout the cascade process. Figure 5b illustrates the temperature fluctuations in FeMnNiCr and Ni. Despite the initial temperature in Ni being higher than that in FeMnNiCr, it quickly stabilizes at a steady state. However, FeMnNiCr exhibits a more gradual temperature decline, mirroring the trend of potential energy variation, and fails to return to 600 K even after 90 picoseconds of cascade evolution. This observation implies that FeMnNiCr has a prolonged thermal peak duration compared to Ni.

To explain the different temperature trends that occur in the two materials, we have calculated the thermal conductivity of the materials. The results show that the thermal conductivity of FeMnNiCr is 5.46 W/m·K, while that of Ni is 35.19 W/m·K, with the latter being about eight times that of the former. Zhang et al. [52] have observed the similar phenomenon through both experimental and computational studies.

Nickel-based alloys exhibit an increase in chemical disorder, which correlates with a substantial reduction in thermal conductivity as the number of constituent elements increases. The elevated chemical disorder in FeMnNiCr contributes to reduced thermal conductivity and prolonged heat dissipation, which in turn extends the thermal peak duration, slows the energy dissipation rate, and allows for greater opportunity for defect migration. This facilitates increased encounter between interstitial atoms and vacancies, leading to a reduction in residual defects within the system at steady state.

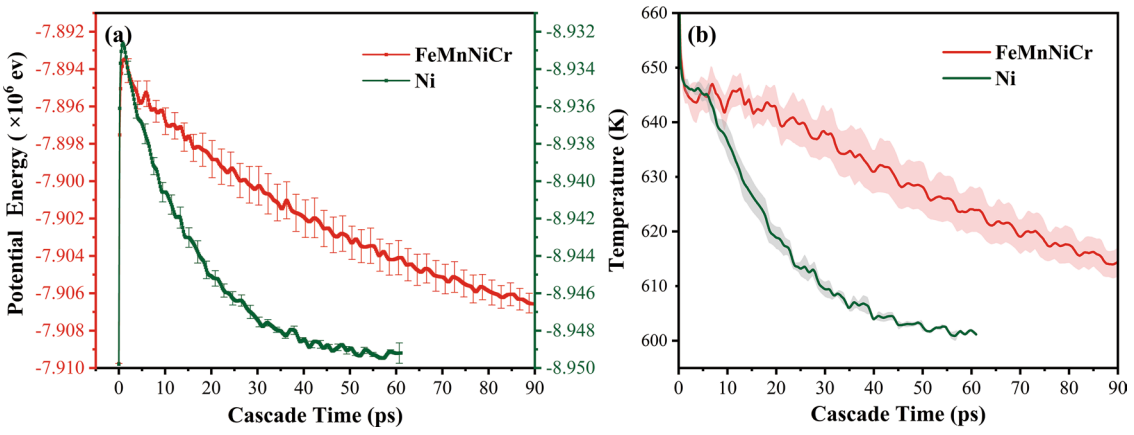

Fig. 5 **a** Potential energy in the FeMnNiCr (red) and Ni (green) during displacement cascades. **b** Temperature of FeMnNiCr and Ni during displacement cascade process

3.4 Migration Properties of Defect Clusters

Figure 3b, d demonstrates that the migration distance of defects in Ni exceeds that in FeMnNiCr under identical initial conditions and PKA energies. To elucidate the divergent defect migration behaviors observed in the two materials, we assess the migration dynamics of defect clusters in Ni and FeMnNiCr by determining their mean free paths. Figure 6 shows the migration trajectories of interstitial clusters, each consisting of 9 atoms, in both materials. In Ni, interstitial clusters exhibit one-dimensional migration along a particular dense row direction, covering greater distances, aligning with prior experimental and simulation studies on the migration patterns of simple metals [20, 53–55]. In contrast, the migration direction of the interstitial clusters in FeMnNiCr shows randomness with shorter migration distances, and exhibits three-dimensional motions, which is similar to that of the migration of NiFe clusters observed experimentally by Lu et al. [4] and the migration of CoNiCrFeMn found by Li et al. [24] in simulation.

Based on the above conclusions, we further explain the different migration modes of interstitial clusters in Ni and FeMnNiCr by the Cage-model [56]. In polyalloys, certain constraints are formed between minor elements randomly distributed in the lattice position, which makes the interstitial clusters exhibit one-dimensional motions in the local spatial range and turn to three-dimensional motions on the constrained surfaces. The Cage-model proposes the interrelationship between the mean free path λ and the proportion of minor elements, c:

$$\lambda = Ac^{-\frac{1}{3}} + B. \tag{3}$$

where A and B are coefficients. In FeMnNiCr, the elements are uniformly and randomly dispersed, resulting in a minor element proportion of 75% for any given element. The Cage model indicates that the mean free path is inversely related to the proportion of minor elements, leading to a notably reduced value. The migration of interstitial clusters within the crystal lattice is markedly constrained. This transition from one-dimensional to three-dimensional migration patterns contributes to the observation of fewer residual defects in FeMnNiCr relative to Ni. In Ni, defects travel greater distances due to one-dimensional migration, reducing the likelihood of interstitial atoms encountering and recombining with vacancies, thus leaving a higher number of defects in the system at equilibrium. Conversely, the three-dimensional motion in FeMnNiCr results in slower defect migration, enhancing the probability of interstitial atoms encountering and recombining with vacancies, thereby substantially decreasing the number of residual defects. Kumar et al. [22] observed that the size of dislocation loops in FeNiMnCr was always small when the irradiation temperature increased from 400 °C to 700 °C in the experiment, which is consistent with our results. In summary, the compositional complexity of FeMnNiCr imparts a reduced mean free path and increased defect complexity, conferring enhanced irradiation resistance compared to Ni.

3.5 Displacement Cascade Simulations Under Prolonged Irradiation

Despite the displacement cascade indicating the superior irradiation resistance of FeMnNiCr over Ni, actual irradiation is a prolonged process that induces substantial alterations in the internal microstructure of material. To enhance our comprehension of the impact of prolonged irradiation on material irradiation resistance, we have conducted further investigations into the evolution of accumulated defects under sustained irradiation conditions.

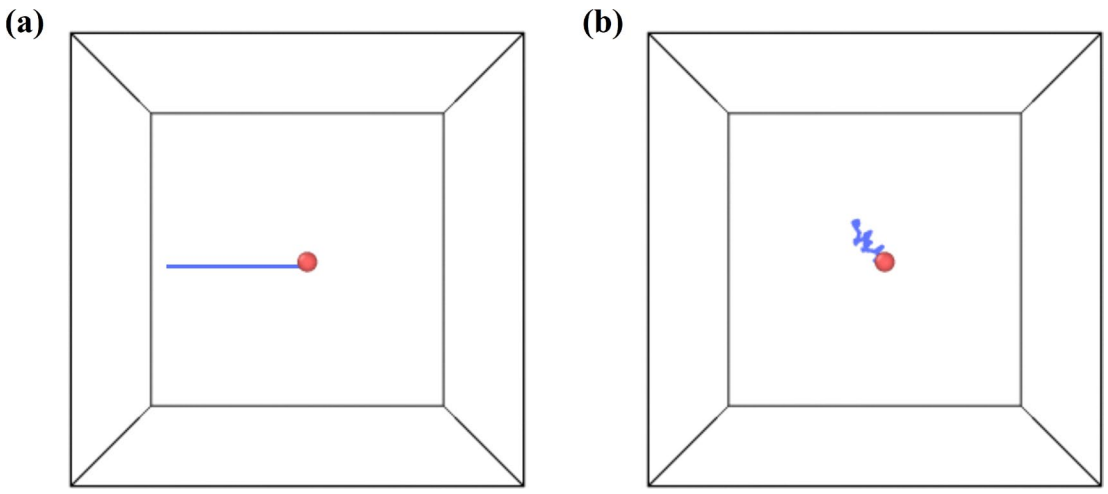

Fig. 6 Migration trajectories of interstitial clusters with 9 atoms: **a** Ni, $T = 800$ K; **b** FeMnNiCr, $T = 1200$ K

Figure 7a, b illustrates the distribution of dislocations resulting from the natural evolution of the two materials with pre-set defects. The findings indicate that point defects in Ni are prone to aggregating, assimilating surrounding minor defects to form stable, large defect clusters that eventually evolve into dislocations. With time, these dislocations become randomly dispersed throughout the system, leading to substantial alterations in the microstructure. Conversely, in FeMnNiCr, the observed dislocation density is markedly reduced, with the majority of defects remaining in the form of small clusters, and the aggregation into larger defect clusters is notably inhibited.

The disparity becomes even more pronounced following the displacement cascade simulations, as depicted in Fig. 7c, d. The number of dislocation in FeMnNiCr rises modestly, whereas in Ni, it experiences a near doubling. By the end of the cascade simulation, the dislocation line length in Ni extends to approximately 275.2 nm, nearly seven times the length of dislocations in FeMnNiCr 42.8 nm. These findings suggest that under prolonged irradiation, defects in FeMnNiCr predominantly exist as small clusters, with fewer large defect clusters forming. Therefore, FeMnNiCr exhibits better irradiation resistance than Ni after prolonged irradiation.

3.6 Evolution of Displacement Cascade Defects in Different High Entropy Alloys

As previously discussed, FeMnNiCr exhibits superior irradiation resistance relative to Ni. Nonetheless, the durability of this advantage in comparison to other high-entropy alloys, renowned for their exceptional anti-irradiation properties, remains to be determined. Therefore, we perform

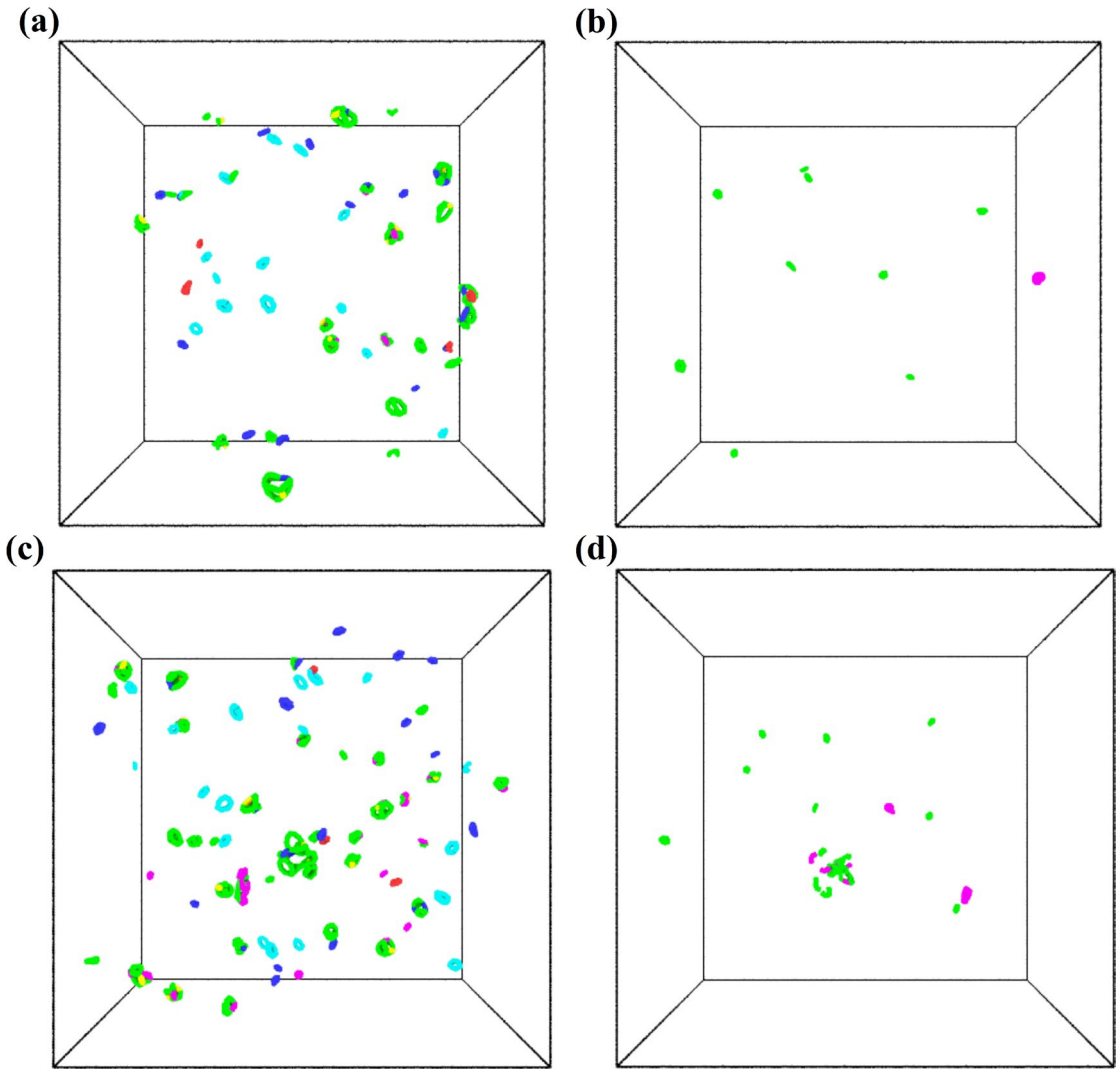

Fig. 7 Dislocation distribution in the system with preset defects at equilibrium: **a** Ni, **b** FeMnNiCr. Dislocation distribution in the system at the end of displacement cascade: **c** Ni, **d** FeMnNiCr

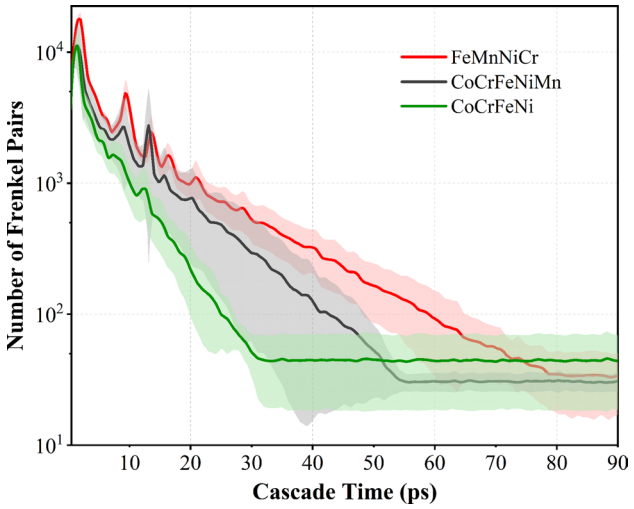

Fig. 8 Evolution of the number of FPs in three HEAs during displacement cascade process. The red, black, and green lines represent the average value

displacement cascade simulations for HEAs with excellent anti-irradiation properties, namely NiCoFeCrMn [23–25], and NiCoCrFe [29–31], in comparison to FeMnNiCr. The simulations for each HEA are both conducted 10 times.

Figure 8 illustrates the evolution of the number of FPs throughout the displacement cascades in the three HEAs. The results show that the HEAs display comparable trends, with FeMnNiCr exhibiting a higher peak defect density relative to the other HEAs, yet it maintains a more extended thermal peak duration. At the end of cascade process, the number of residual defects follows the order: CoCrFeNiMn < FeMnNiCr < CoCrFeNi. Although the number of residual defect number in FeMnNiCr is marginally higher than that in CoVrFeNiMn, the discrepancy is minimal. Furthermore, the absence of Co elements in FeMnNiCr mitigates the risk associated with its application, rendering it a highly promising candidate for nuclear structure materials.

4 Summary

This study employs molecular dynamics simulations to investigate the displacement cascade process in the cobalt-free high-entropy alloy FeMnNiCr at a high-temperature irradiation environment of 600 K, comparing its behavior with that of Ni and other HEAs. The study examines the evolution of point defects induced by the displacement cascade effect and the distribution patterns of residual defects in FeMnNiCr. The study elucidates the following three microscopic mechanisms contributing to the remarkable irradiation resistance of FeMnNiCr.

First, FeMnNiCr has prolonged thermal peak durations during irradiation, accompanied by a slower rate of energy dissipation. This characteristic extends the time frame within which interstitial and vacancy defects can encounter and recombine within the material.

Second, the interstitial clusters of FeMnNiCr have a relatively shorter mean free path, displaying three-dimensional spatial migration tendencies. This leads to a more concentrated defect distribution in space, significantly enhancing the encounter rate between defects, thereby facilitating a more efficient defect annihilation process and minimizing the residual defect population.

A last, under prolonged irradiation, defects in FeMnNiCr predominantly manifest as small clusters compared to Ni. Other HEAs, FeMnNiCr and NiCoFeCrMn exhibit similar residual defect profiles to FeMnNiCr post-displacement cascade. Given the absence of cobalt in FeMnNiCr, it holds promise for applications in nuclear structure materials.

Our atomistic insights into the mechanisms of the irradiation resistance of FeMnNiCr might be helpful in material design of the next-generation reactor structure materials in nuclear energy.

Acknowledgements The work is supported by the Fundamental Research Funds for the Central Universities (No. FRF-IDRY-20-008). Q. P. acknowledges the support provided by the National Natural Science Foundation of China (Grant No. 12272378), the High-level Innovation Research Institute Program of Guangdong Province (Grant No. 2020B0909010003), and the LiYing Program of the Institute of Mechanics, Chinese Academy of Sciences (Grant No. E1Z1011001).

Data availability The raw/processed data required to reproduce these findings are available on request from the authors.

Declarations

Conflict of interest The authors state that there are no conflicts of interest to disclose.

References

[1] S.J. Zinkle, J.T. Busby, Mater. Today **12**, 12 (2009)
[2] C.M. Lousada, I.L. Soroka, Y. Yagodzinskyy, N.V. Tarakina, O. Todoshchenko, H. Hänninen, P.A. Korzhavyi, M. Jonsson, Sci. Rep. **6**, 24234 (2016)
[3] B. Uberuaga, R. Hoagland, A. Voter, S. Valone, Phys. Rev. Lett. **99**, 135501 (2007)
[4] B. Gludovatz, A. Hohenwarter, D. Catoor, E.H. Chang, E.P. George, R.O. Ritchie, Science **345**, 1153 (2014)
[5] C. Li, X. Hu, T. Yang, N.K. Kumar, B.D. Wirth, S.J. Zinkle, J. Nucl. Mater. **527**, 151838 (2019)
[6] J. Yang, K. Shi, Q. Chen, W. Zhang, C. Zhu, Z. Ning, J. Liao, Y. Yang, N. Liu, J. Yang, Surf. Coat. Technol. **418**, 127252 (2021)
[7] S.J. Zinkle, G. Was, Acta Mater. **61**, 735 (2013)
[8] Y. Guérin, G.S. Was, S.J. Zinkle, MRS Bull. **34**, 10 (2009)
[9] J.W. Yeh, S.K. Chen, S.J. Lin, J.Y. Gan, T.S. Chin, T.T. Shun, C.H. Tsau, S.Y. Chang, Adv. Eng. Mater. **6**, 299 (2004)

[10] B. Cantor, I. Chang, P. Knight, A. Vincent, Mater. Sci. Eng. A **375**, 213 (2004)
[11] W. Li, P.K. Liaw, Y. Gao, Intermetallics **99**, 69 (2018)
[12] Z. Lei, X. Liu, Y. Wu, H. Wang, S. Jiang, S. Wang, X. Hui, Y. Wu, B. Gault, P. Kontis, Nature **563**, 546 (2018)
[13] T. Yang, Y. Zhao, Y. Tong, Z. Jiao, J. Wei, J. Cai, X. Han, D. Chen, A. Hu, J. Kai, Science **362**, 933 (2018)
[14] M.H. Chuang, M.H. Tsai, W.R. Wang, S.J. Lin, J.W. Yeh, Acta Mater. **59**, 6308 (2011)
[15] V. Gavriljuk, B. Shanina, H. Berns, Acta Mater. **56**, 5071 (2008)
[16] C. Liu, Y. Wang, Y. Zhang, L. Wang, Acta Metall. Sin. -Engl. Lett. **37**, 3 (2024)
[17] J.Q. Zheng, M.L. Wang, W.N. Jiao, L.J. Zou, Y. Di, Acta Metall. Sin. -Engl. Lett. **36**, 1493 (2023)
[18] M.H. Tsai, J.W. Yeh, Mater. Res. Lett. **2**, 107 (2014)
[19] Y. Dou, K. Jin, X. He, W. Yang, W. Zhong, H. Cao, C. Huang, At. Energy Sci. Technol. **53**, 1868 (2019)
[20] C. Lu, L. Niu, N. Chen, K. Jin, T. Yang, P. Xiu, Y. Zhang, F. Gao, H. Bei, S. Shi, Nat. Commun. **7**, 13564 (2016)
[21] L. Yang, H. Ge, J. Zhang, T. Xiong, Q. Jin, Y. Zhou, X. Shao, B. Zhang, Z. Zhu, S. Zheng, J. Mater. Sci. Technol. **35**, 300 (2019)
[22] N.K. Kumar, C. Li, K. Leonard, H. Bei, S. Zinkle, Acta Mater. **113**, 230 (2016)
[23] Y. Li, R. Li, Q. Peng, Nanotechnology **31**, 025703 (2019)
[24] Y. Li, R. Li, Q. Peng, S. Ogata, Nanotechnology **31**, 425701 (2020)
[25] Z. Su, T. Shi, H. Shen, L. Jiang, L. Wu, M. Song, Z. Li, S. Wang, C. Lu, Scr. Mater. **212**, 114547 (2022)
[26] R. Li, L. Guo, Y. Liu, Q. Xu, Q. Peng, Acta Metall. Sin. -Engl. Lett. **36**, 1482 (2023)
[27] R. Li, Y. Li, Y. Liu, Q. Peng, Comput. Mater. Sci. **225**, 112185 (2023)
[28] B. Kombaiah, Y. Zhou, K. Jin, A. Manzoor, J.D. Poplawsky, J.A. Aguiar, H. Bei, D.S. Aidhy, P.D. Edmondson, Y. Zhang, A.C.S. Appl, Mater. Interfaces **15**, 3912 (2023)
[29] Y. Lin, T. Yang, L. Lang, C. Shan, H. Deng, W. Hu, F. Gao, Acta Mater. **196**, 133 (2020)
[30] W. Lin, G. Yeli, G. Wang, J. Lin, S. Zhao, D. Chen, S. Liu, F. Meng, Y. Li, F. He, J. Mater. Sci. Technol. **101**, 226 (2022)
[31] D. Chen, Y. Tong, H. Li, J. Wang, Y. Zhao, A. Hu, J. Kai, J. Nucl. Mater. **501**, 208 (2018)
[32] T. Shi, P.H. Lei, X. Yan, J. Li, Y.D. Zhou, Y.P. Wang, Z.X. Su, Y.K. Dou, X.F. He, D. Yun, Tungsten **3**, 197 (2021)
[33] Z. Wu, H. Bei, Mater. Sci. Eng. A **640**, 217 (2015)
[34] D.J. Bacon, F. Gao, Y.N. Osetsky, J. Nucl. Mater. **276**, 1 (2000)
[35] R. Wang, Z. Chen, Y. Shu, Y. Lin, Z. Liu, H. Deng, W. Hu, T. Yang, J. Nucl. Mater. **577**, 154342 (2023)
[36] L. Qian, H. Bao, R. Li, Q. Peng, Mater. Adv. **3**, 1680 (2022)
[37] Q. Fang, J. Peng, Y. Chen, L. Li, H. Feng, J. Li, C. Jiang, P.K. Liaw, Mech. Mater. **155**, 103744 (2021)
[38] J. Dong, X. Feng, X. Hao, W. Kuang, Scr. Mater. **204**, 114127 (2021)
[39] A.P. Thompson, H.M. Aktulga, R. Berger, D.S. Bolintineanu, W.M. Brown, P.S. Crozier, S.J. Plimpton, LAMMPS-a flexible simulation tool for particle-based materials modeling at the atomic, meso, and continuum scales. Comput. Phys. Commun. **271**, 108171 (2022)
[40] W.M. Choi, Y.H. Jo, S.S. Sohn, S. Lee, B.J. Lee, npj Comput. Mater. **4**, 1 (2018)
[41] H.S. Do, B.J. Lee, Sci. Rep. **8**, 16015 (2018)
[42] J.F. Ziegler, J.P. Biersack, in Treatise on Heavy-Ion Science: Volume 6: Astrophysics, Chemistry, and Condensed Matter, ed. by D.A. Bromley (Springer US, Boston, MA, p. 93) (1985)
[43] Y. Zhang, G.M. Stocks, K. Jin, C. Lu, H. Bei, B.C. Sales, L. Wang, L.K. Béland, R.E. Stoller, G.D. Samolyuk, Nat. Commun. **6**, 8736 (2015)
[44] W. Chen, X. Ding, Y. Feng, X. Liu, K. Liu, Z.P. Lu, D. Li, Y. Li, C.T. Liu, X.Q. Chen, J. Mater. Sci. Technol. **34**, 355 (2018)
[45] A. Stukowski, Modell. Simul. Mater. Sci. Eng. **20**, 045021 (2012)
[46] K. Nordlund, M. Ghaly, R. Averback, M. Caturla, T.D. de La Rubia, J. Tarus, Phys. Rev. B **57**, 7556 (1998)
[47] A. Stukowski, V.V. Bulatov, A. Arsenlis, Modell. Simul. Mater. Sci. Eng. **20**, 085007 (2012)
[48] Z. Sun, C. Shi, L. Gao, S. Lin, W. Li, J. Alloys Compd. **901**, 163554 (2022)
[49] A. Calder, D.J. Bacon, A.V. Barashev, Y.N. Osetsky, Philos. Mag. **90**, 863 (2010)
[50] C. Lu, T. Yang, K. Jin, N. Gao, P. Xiu, Y. Zhang, F. Gao, H. Bei, W.J. Weber, K. Sun, Acta Mater. **127**, 98 (2017)
[51] K. Jin, C. Lu, L. Wang, J. Qu, W. Weber, Y. Zhang, H. Bei, Scr. Mater. **119**, 65 (2016)
[52] Y. Zhang, K. Jin, H. Xue, C. Lu, R.J. Olsen, L.K. Beland, M.W. Ullah, S. Zhao, H. Bei, D.S. Aidhy, J. Mater. Res. **31**, 2363 (2016)
[53] Y. Matsukawa, S.J. Zinkle, Science **318**, 959 (2007)
[54] A. Foreman, W. Phythian, C. English, Philos. Mag. A **66**, 671 (1992)
[55] P. Zhao, Y. Shimomura, Comput. Mater. Sci. **14**, 84 (1999)
[56] C. Lu, T. Yang, L. Niu, Q. Peng, K. Jin, M.L. Crespillo, G. Velisa, H. Xue, F. Zhang, P. Xiu, J. Nucl. Mater. **509**, 237 (2018)